

A Microphysiological System Combining Electrospun Fibers and Electrical Stimulation for the Maturation of Highly Anisotropic Cardiac Tissue

Adrián López-Canosa^{1,2}, Soledad Perez-Amodio^{1,2,3}, Eduardo Yanac-Huertas^{1,2}, Jesús Ordoño^{1,2}, Romen Rodriguez-Trujillo^{4,5,6}, Josep Samitier^{5,4,2,6}, Oscar Castano^{4,1,2,6,*} and Elisabeth Engel^{1,2,3}

¹Biomaterials for Regenerative Therapies, Institute for Bioengineering of Catalonia (IBEC), The Barcelona Institute of Science and Technology (BIST), Baldiri i Reixac 10-12, 08028 Barcelona, Spain.

²CIBER en Bioingeniería, Biomateriales y Nanomedicina (CIBER-BBN) 28029 Madrid, Spain.

³IMEM-BRT Group, Dept. Materials Science and Engineering, EEBE, Technical University of Catalonia (UPC), 08019 Barcelona, Spain.

⁴Electronics and Biomedical Engineering, Universitat de Barcelona (UB), 08028 Barcelona, Spain.

⁵Nanobioengineering group, Institute for Bioengineering of Catalonia (IBEC) Barcelona Institute of Science and Technology (BIST), 12 Baldiri i Reixac 15-21, Barcelona 08028, Spain.

⁶Institute of Nanoscience and Nanotechnology, Universitat de Barcelona (UB), 08028 Barcelona, Spain.

e-mail: oscar.castano@ub.eu

Abstract

The creation of cardiac tissue models for preclinical testing is still a non-solved problem in drug discovery, due to the limitations related to the *in vitro* replication of cardiac tissue complexity. Among these limitations, the difficulty of mimicking the functional properties of the myocardium due to the immaturity of the used cells hampers the obtention of reliable results that could be translated into human patients. *In vivo* models are the current gold standard to test new treatments, although it is widely acknowledged that the used animals are unable to fully recapitulate human physiology, which often leads to failures during clinical trials.

In the present work, we present a microfluidic platform that aims to provide a range of signaling cues to immature cardiac cells to drive them towards an adult phenotype. The device combines topographical electrospun nanofibers with electrical stimulation in a microfabricated system. We validated our platform using a co-culture of neonatal

mouse cardiomyocytes and cardiac fibroblasts, showing that it allows us to control the degree of anisotropy of the cardiac tissue inside the microdevice in a cost-effective way. Moreover, a 3D computational model of the electrical field was created and validated to demonstrate that our platform is able to closely match the distribution obtained with the gold standard (planar electrode technology) using inexpensive rod-shaped biocompatible stainless-steel electrodes. The functionality of the electrical stimulation was shown to induce a higher expression of the tight junction protein Cx-43, as well as the upregulation of several key genes involved in conductive and structural cardiac properties. These results validate our platform as a powerful tool for the tissue engineering community due to its low cost, high imaging compatibility, versatility, and high-throughput configuration capabilities.

Keywords: Microphysiological system, In vitro models, Heart-on-a-chip, Cardiac tissue engineering, Electrospinning.

1. Introduction

The cardiac muscle is a highly organized and specialized tissue in which electrical signals are translated into synchronized fiber contractions that result in the pumping action of the heart ¹. One of the overarching goals of cardiac research is to create an *in vitro* model that closely resembles the myocardium in order to perform developmental, disease studies, and drug testing ². Traditional cell culture methods are limited in replicating the complexity of the native cardiac niche, as they do not usually incorporate any of the cues present in the actual microenvironment that drive tissue development ³. Recent advancements in microfabrication technologies have revolutionized the field of cardiac tissue research, providing new tools to manipulate the cellular microenvironment and spatiotemporal signaling with unprecedented control levels, which drastically minimizes the differences between the *in vitro* and *in vivo* models ⁴.

These microfluidic cell-culture models, commonly referred to as microphysiological systems (MPS) or organs-on-a-chip, allow the researchers to incorporate many of the

guiding cues found in the actual *in vivo* milieu in a more efficient way than macroscale bioreactors. For instance, the experimental costs are drastically reduced due to the lower number of cells and reagents required, which also translates into an increased experimental throughput ⁵. From the different stimuli that can be used to guide cardiac assembly *in vitro*, the spatial cues are crucial, as they are required to mimic the high anisotropy of native myocardium. This aligned structure of cardiac fibers is needed for optimal electrical signal propagation and the subsequent generation of the contractile force in the heart ⁶. Although different studies are reporting the creation of aligned cardiac tissues in 3D ⁷⁻⁹, there is still a lack of robust technologies that permit the creation of these patterns inside of matrices such as hydrogels compatible with microsize devices. Therefore, 2D models remain the preferred option to perform the studies, especially for drug screening purposes ¹⁰. Current strategies to mimic anisotropic cardiac tissue architectures in 2D can be mainly grouped into four categories.

Current strategies to mimic anisotropic cardiac tissue architectures in 2D are mainly based on the use of microcontact printing ^{11,12} to generate patterned surfaces such as lanes ^{13,14}; the use of microfluidic channels that are reversibly bonded to a certain substrate to then perfuse and crosslink a hydrogel in just some selected areas ¹⁵⁻¹⁷, or creating microgrooves on the substrate using different fabrication techniques such as microabrasion ¹⁸ or hot embossing ¹⁹. An interesting approach relies on the use of nanofibrous scaffolds fabricated by electrospinning ²⁰. This technique offers the advantage that provides topographical cues resembling the native ECM of the heart and allows the manipulations of different microarchitecture parameters (such as fiber orientation, composition, fiber thickness, fiber density,...) ²¹. Several materials such as collagen ²², polymethylglutarimide (PMGI) ²¹, polylactic-co-glycolic acid (PLGA) ²³ or polyacrylonitrile (PAN) ²⁴ have been reported to improve the functionality of the cardiac constructs not only for drug testing purposes but also for the generation of cardiac patches for implantation to treat post-myocardial infarction injuries.

Other essential cues for cardiac maturation are the electrical and mechanical signals, as in the native heart, the myocardium expands as blood enters each chamber, followed by an electrical signal that causes cellular contraction²⁵. Several studies have shown the effects of static^{9,26} or cyclic^{27,28} mechanical stretch on the improvement of the functional and structural properties of tissue constructs. However, electrical stimulation is generally considered a more biomimetic way to induce mechanical stimulation (compared to stretching), as *in vivo* it occurs via excitation-contraction coupling¹⁰. Its influence on cardiac tissue maturation and organization was first shown on neonatal rat cardiomyocytes (CM) seeded in a porous collagen scaffold, resulting in well-defined sarcomeric structures and polarization of gap junctional proteins towards the end of the membrane among other features²⁹. From that pioneering work, well-established protocols for delivering pulsatile electrical fields have been developed^{30,31}, and many studies have incorporated electrical stimulation to mature cardiac constructs, either in macroscale^{32–36} or microscale^{19,37–39} bioreactors.

In this work, we report the development of a MPS combining topographical signaling cues created with electrospun nanofibers with electrical stimulation in a microfabricated system. The significance of this work relies on the possibility to incorporate both cues in a robust, reproducible, and cost-effective system. The final device is conceived as an easy-to-use platform that can be of great value for the cardiac research community, due to its low cost, high imaging compatibility, versatility, and high-throughput configuration capabilities. To achieve this goal, we propose a method to deposit electrospun fibers on thin commercial coverslips and bond them to a microfluidic device made in polydimethylsiloxane (PDMS). We also characterized this substrate and developed an experimentally validated computational model of the device to optimize the best electrical stimulation configuration, in terms of magnitude and uniformity, in the cell chamber region. As proof of the functionality of the system, we co-cultured cardiac fibroblasts and cardiomyocytes from neonatal CD1 mice and quantified cell orientation and elongation by immunostaining for specific cardiac markers (such as troponin T). In addition, the

maturation of the developed construct was analyzed using specific genes involved in the conductive and contractile properties of cardiac tissues by real-time polymerase chain reactions (qRT-PCR).

2. Materials and methods

2.1. Electrospinning and characterization of the nanofibers

Poly-L/DL lactic acid 70/30 (PLA 70/30) (Purasorb PLDL 7038, viscosity 3.8 dl/g at 25 °C, Purac Biomaterials, NL) was dissolved at 8 % w/w in 2,2,2-trifluoroethanol (99.8 %, Panreac, ES). To acquire fluorescent nanofibers, rhodamine B (Sigma, DE) was also added at a final non-cytotoxic concentration of 0.01 % w/v. The solution was loaded into a 5 ml syringe (Becton-Dickinson, US) and delivered through a 21-gauge blunt-tip needle (Nordson EFD, US) at a flow rate of 0.5 ml/h using a syringe pump (NE-300, New Era Inc, USA). Fibers were electrospun using a high-voltage power supply (NanoNC, KR) onto a grounded stationary collector placed at a distance of 20 cm from the tip of the syringe. The collector was round in shape, with a diameter of 9 cm, and around which we wrapped pieces of aluminum foil of 20x33 cm with three 0.17 mm coverslips (Deltalab, ES) secured with tape following the middle axis of the rectangle. To obtain randomly distributed fibers, the collector was kept static for 2 min and the power supply configured at 9 kV, while for the aligned fibers the collector was set at a rotating speed of 1000 rpm for 6 min with a potential of 12 kV. A focusing ring-shaped electrode was also used in the latter case to restrict the deposition area of the electrospinning jet.

The morphology of the fibers was assessed using a field emission scanning electron microscope (NOVA Nano SEM 230, Fei Co., NL) operating at 10 kV and covered with an ultra-thin gold layer (10 nm) deposited by thermal evaporation (Univex 450B, Oerlikon Leybold Vacuum, DE). SEM images were processed in Image J (NIH, US) to obtain different parameters of interest. To obtain fiber alignment information, the Oval Profile ImageJ ^{40,41} plugin was used. Briefly, it performs an oval projection of the Fast Fourier Transform (FFT) of the images followed by a radial summation of the pixel intensities for

each angle between 0 and 180° (as de FFT data are symmetric). The degree of alignment is reflected by the height and shape of the peak, which indicates the principal angle of orientation. The mean fiber diameter and the standard deviation were also assessed by performing 18 measurements on both random and aligned samples. Finally, the stiffness of the fibers was assessed by calculating the approached elastic modulus in a tensile strain assay using a Zwick-Roell Zwicki-line Z0.5TN universal testing machine (Zwick-Roell, DE) and a 10 N force cell. The number of replicates was 5 and the speed of assay was set to 10 mm/min.

2.2. Device design and fabrication

The microfluidic platform design (see **Fig.1-a-c**) was performed using CAD software (AutoCAD 2019) and consists of a main cell culture chamber (1300 μm wide, 8800 μm long, 150 μm high) flanked by two media channels (750 μm wide, 150 μm high). There are also four 1.2 mm holes tangent to the media channels to place the rod-shaped electrodes needed to electrically stimulate the cardiac cells. Master molds were fabricated in a cleanroom environment using standard photolithography techniques with a SU8-3050 photoresist (MicroChem) and 4" silicon wafers as substrates. Polydimethylsiloxane (PDMS, Sylgard 184, Dow Corning) elastomer was mixed at a ratio of 10:1 w/w (base: curing agent). After degassing and curing overnight at 65 °C, the PDMS was peeled off from the master, cut into individual devices, and punched. We made 6 mm diameter holes for the media reservoirs and 1.2 mm holes for the cell chamber inlets and electrode holes. Devices were cleaned and bonded to coverslips (0.17 mm thickness) by treating them in an air plasma chamber (Harrick Plasma PCD-002-CE) for 30 s at 10.5 W. As previously explained, the coverslips were patterned with electrospun nanofibers in either a random or aligned fashion. Due to the high hydrophobicity of the PLA 70/30 ⁴², we removed most of the unused deposited fibers before the plasma treatment with a cloth bathed in acetone, leaving just an area slightly bigger than the cell culture chamber. That way, the PDMS frame acted as a holder for

the fibers so they remained in a fixed position. Finally, all the chips were thermally treated for 2 h at 85 °C to stabilize the bonding. We were aware that the glass transition temperature (T_g) of PLA electrospun fibers ranges 57-58 °C⁴³. However, we did not observe any effect on the topography of the fibers. Then, all chips were sterilized by putting them under UV light for at least 30 min.

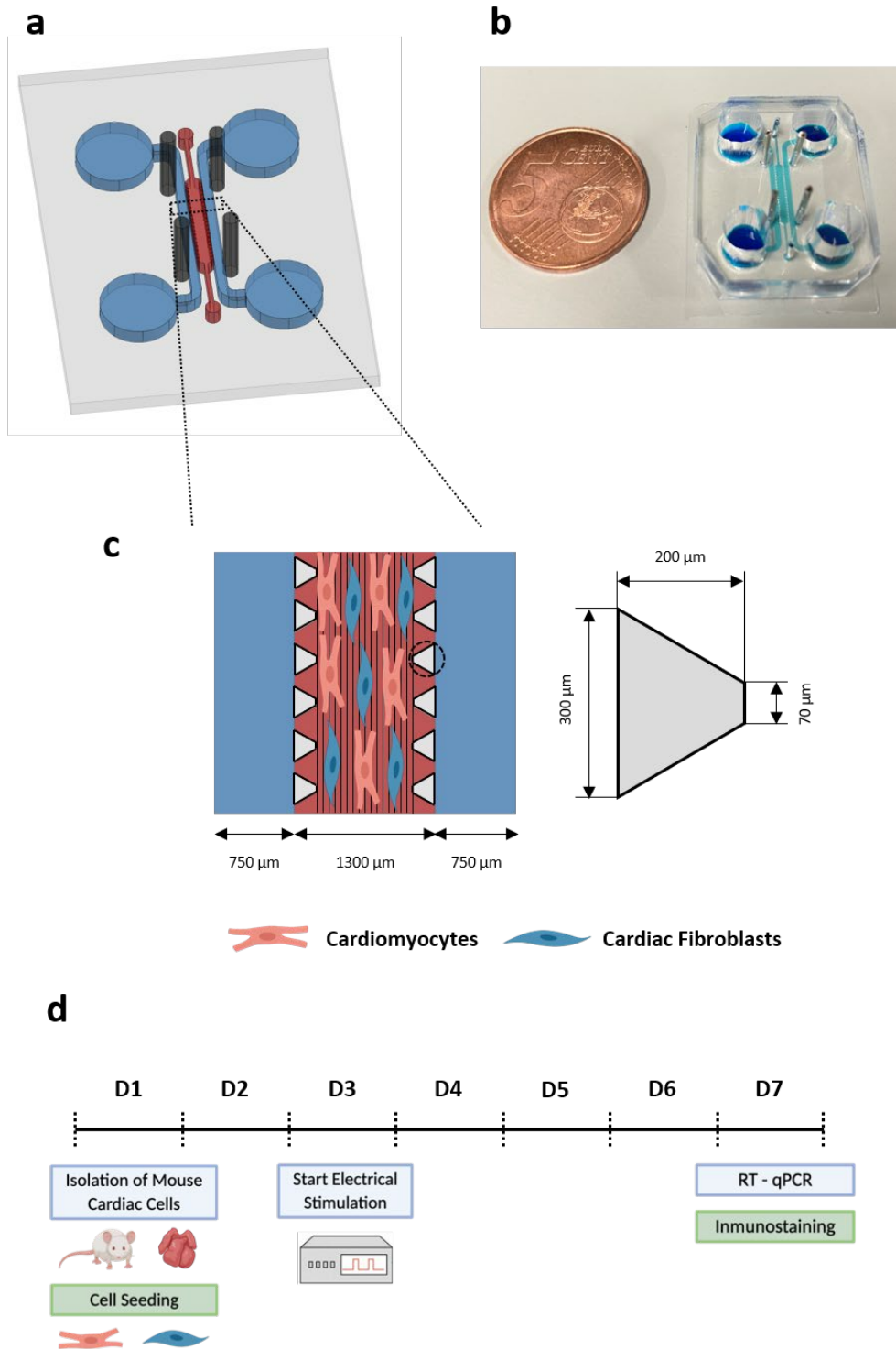


Figure 1 Design and cell culture model of the microfluidic platform for the generation and maturation of highly anisotropic cardiac tissue. (a) Schematic representation of the microfluidic device including the cell chamber (red), the media channels (blue), and the stimulation electrodes (dark gray). (b) Photo of the assembled microfluidic platform. (c) Detailed schematic view showing the patterned substrate created with electrospun fibers in the cell chamber and how the cardiac cells follow its orientation. A detail of micropost geometry and dimensions is also provided. (d) Experimental timeline.

2.3. Finite element modeling of the electrical field

A computational model of our microfluidic platform was developed using the finite element method (FEM) to obtain the distribution and magnitude of the electric field. The area of interest considered corresponds to the cell chamber located between the two pairs of rod-like electrodes and in which the cells are seeded and grown as a monolayer (area $\approx 11.4 \text{ mm}^2$). The 3D geometry of the device was divided into three different homogenous domains: (1) the fluid domain representing the culture medium, (2) the stainless steel electrodes, and (3) the PDMS frame and posts, each with their respective electrical properties ³³ (see table 1).

Table 1. Electrical properties of the three domains within the MPS.

Materials	Conductivity (σ) [S/m]	Permittivity (ϵ)
Culture media	1.5	80.1
PDMS	$1 \cdot 10^{-22}$	2.63
Stainless steel	$1.32 \cdot 10^6$	1.005

The electric field distribution was computed with the software COMSOL Multiphysics 5.5 (Comsol Inc., US). Numerical simulations were performed using the *Electric Current* interface, assuming direct-current (DC), steady-state conditions to solve Maxwell's equations, for which the governing equation is:

$$-\nabla \cdot (\sigma \nabla V - J_e) = Q_i$$

Where V is the electric potential, σ is the electric conductivity, J_e is the generated current density and Q_i is the local current source. The electric field can be derived from the potential V obtained in the aforementioned equation as $E = -\nabla V$ assuming electroquasistatic conditions. Regarding the boundary conditions, one pair of the stainless-steel electrodes were grounded, while the other pair was set to the different

electric potentials. The electrospun coated glass surface was considered as an electrically insulating boundary condition. The geometry was discretized with a tetrahedral mesh with approximately 40,000 elements and calculated using a direct solver based on the PARDISO method. Mesh sensitivity studies were conducted to ensure consistency of the results.

2.4. Validation of the electrical model

In order to validate the computational model of the electrical stimulation, electrical signal recordings were performed in different places inside the microfluidic system. We used a variation of the design with the electrodes placed at 1 mm from the cell chamber inlets to avoid measurement problems, such as the accidental contact of the voltage probe with the electrodes. To perform the measurements, holes were made during the fabrication of PDMS devices used for this test in three different positions of the cell chamber: (1) between the 2nd and 4th rows of posts starting from one of the inlets of the cell chamber, (2) between the 9th and 11th rows of posts from the chosen inlet and, (3) between the 2nd and 4th rows of posts starting from the opposing inlet (**see section 3.2**). The chip was filled with PBS (100 μ l/reservoir) and the stimulation electrodes were placed in their corresponding holes and connected to a function generator (Agilent 33250A, US) using a coaxial-alligator cable. One pair of electrodes on one side of the chamber was grounded, while in the other pair a biphasic wave was applied to range from -2.5 V during 1 ms to +2.5 V during another 1 ms (so $V_{pp} = 5$ V and the total duration of 2 ms). The frequency of the signal was set at 1 Hz. To perform the measurements, a stainless-steel needle was connected to a digital oscilloscope (Keysight DSOX 3024T, US) and used as a voltage probe in each of the holes made in the device. The measurements were performed in a total of three independent devices.

2.5. Isolation and seeding of mouse cardiac cells

Cardiac primary cells were obtained from CD1 neonatal mice as previously described⁴⁴. Hearts from 1-3-day-old mice were extracted and transferred on ice into a solution of

PBS with 20 mM 2,3-butanedione monoxime (BDM, Sigma, DE), where they were cleaned and minced into small pieces using curved scissors (approximately 0.5-1 mm³ or smaller). Then, tissue fragments underwent a predigestion step by incubating in a trypsin-EDTA solution at 0.25 % (Sigma, DE) with 4 µg/mL of DNase I and 20 mM BDM and subjected to 20-25 cycles of enzymatic digestion using collagenase II (Thermo Fisher, US) and dispase II (Sigma, DE) in L-15 medium (Sigma, DE) with 20 mM BDM. Pooled supernatants were collected through a 70 µm nylon cell strainer (Corning, US) and centrifuged at 200 G for 10 min. The pellet was resuspended in DMEM containing 1 g/L glucose (Thermo Fisher, US) supplemented with a 19 % of M-199 medium (Sigma, DE), 10 % horse serum (Sigma, DE), 5 % fetal bovine serum (Sigma, DE), and 1% penicillin and streptomycin (Thermo Fisher, US). The cell suspension was plated into a cell culture dish in order to separate most of the non-myocytic cell fraction of the heart and avoid excessive proliferation in subsequent experiments. After 1 h of incubation, the supernatant containing a purified population of cardiomyocytes was collected in a 0.5 ml Eppendorf.

2.6. Cell culture and electrical stimulation

Isolated cardiac cells were centrifuged and resuspended at a density of 20×10^6 cells/ml in culture media, which is composed of DMEM containing 4.5 g/L glucose (Thermo Fisher, US) supplemented with 17% of M-199 medium (Sigma, DE), 4 % horse serum (Sigma, DE) and 1% penicillin and streptomycin (Thermo Fisher, US). Before cell seeding, all devices were coated with porcine gelatin (Sigma, DE) at 0.5 % w/v in distilled water for 1 h at 37 °C. Approximately 10 µl of the cell suspension (~200.000 cells/device) were injected into the microfluidic system and incubated at 37 °C for approximately 4 hours to allow cell attachment. Then, the chip channels were hydrated by adding 60 µl of cell culture media in each of the reservoirs of one side of the chamber and gently aspirating from the other end with a 1 ml pipette with the tip cut to fit the size of the reservoirs. Finally, each reservoir was filled with medium (approximately 120 µl) and

each chip was kept inside a 100 mm Petri dish in a 37° C, 5 % CO₂ incubator with daily changes of media for the duration of the experiment (7 days).

Electrical stimulation was started on day 3 to provide cells enough time to recover from the isolation procedure. To apply the stimulation, AISI 304 stainless steel electrodes were made by machining 20G microlance needles (Becton Dickinson, US), yielding cylinders of 0.86-0.92 mm in diameter and 2 cm in length, which fitted into the 1 mm dedicated holes of the device. An alligator clip was clamped to each pair of electrodes and then connected to a coaxial-alligator cable coming from a function generator (Agilent 33250A, US). A small groove was machined in the Petri dishes to easily take the cables out. A biphasic wave of $V_{pp} = 5$ V, 2 ms in width, and a frequency of 1 Hz was applied, which are the recommended parameters according to the most established protocols^{30,31}. The electrical stimulation was maintained for 5 days before the final readouts (see the experimental timeline in **Fig.1-d**).

2.7. Immunostaining, quantification of cell alignment, and Cx-43 expression

Cardiac cells were fixed after 7 days in culture with 4 % paraformaldehyde (Electron Microscopy Sciences, US) for 15 minutes after washing cells twice with sterile 1x PBS. Then, they were washed again with 1x PBS and permeabilized with a solution of Triton X-100 (Sigma, DE) at 0.1 % v/v in 1x PBS with glycine (Sigma, DE) at 0.15 % w/v (PBS-gly) for 15 min. After that, cells were treated for 2 h with a blocking solution of bovine serum albumin (Sigma, DE) at 5 % w/v in PBS-gly to prevent non-specific antibody bindings. Samples were then incubated overnight at 4 °C with rabbit polyclonal antibody against connexin-43 (Abcam ab11370, UK) (1:400) in blocking solution and mouse monoclonal antibody against cardiac troponin T (Abcam ab8295, UK) (1:200). The next day, samples were incubated for 2 h at room temperature with Alexa 488 against mouse antibody (Abcam ab150117, UK) and Alexa 635 against a rabbit antibody (Thermo Fisher, US), both at 1:200 in blocking solution. A counterstaining for cell nuclei was also performed incubating DAPI (Thermo Fisher, US) (1:1000) in PBS-gly for 10 min at room

temperature. Samples were then rinsed three times in PBS-gly and maintained at 4 °C in the same solution until image acquisition.

Imaging was performed on a Leica Thunder fluorescence microscope (Leica Microsystems, DE) with the same acquisition parameters for all the samples (exposure time, LED power, etc.) and the obtained images were processed using Image J software⁴⁵ (NIH, US). To quantify cell alignment, we used the plugin *Orientation J* to obtain the orientation and isotropy properties of the images based on the evaluation of the gradient structure tensor⁴⁶. The expression of the protein connexin-43 was also estimated from the acquired images. Briefly, the procedure consists of removing the background illumination of the DAPI and Cx-43 images, converting them to grayscale, and then binarizing them by applying automated thresholding based on the Otsu method. Finally, the number of objects for each image is labeled and counted using the *Analyze Particles* plugin of Image J. The amount of Cx-43 dots is divided by the number of cell nuclei, which results in a normalized core for the quantity of gap junction proteins per cell. Two images per device from a total of three replicates were considered for each of the two experimental conditions (random fibers without electrical stimulation and aligned fibers with electrical stimulation).

2.8. Real-time quantitative PCR

qRT-PCR analyses were performed for a range of cardiac markers using the StepOnePlus RT-PCR System (AB Applied Biosystems Life Technologies, US). To isolate RNA from our microfluidic system, cells were thoroughly washed with sterile 1x PBS (five washing steps with 4 min intervals of incubation) to remove all traits of phenol red present in the cell culture media and avoid further interference in downstream reactions. Then, a buffer provided in the RNeasy Plus Micro kit (Qiagen, NL) was used to lyse the cells (60 µl per upstream reservoir followed by a 5 min incubation). The lysate was then collected from one of the cell chamber inlets into a 0.5 Eppendorf vial and homogenized vortexing it for 1 min. The remaining isolation steps were performed

following the manufacturer's protocols, including the removal of gDNA. The quality and concentration of the extracted RNA samples were assessed using a Nanodrop 1000 spectrophotometer (Thermo Fisher, US). After this step, the RNA was transcribed into cDNA using the RT² First Strand Kit (Qiagen, NL) and real-time PCR performed with the RT² SYBR Green Mastermix (Qiagen, NL) following the manufacturer's protocols. Specific primers for amplifying TNNI3, GJA1, and MYH6, MYH7, and housekeeping gene R18S were used (Qiagen, NL). Data obtained by qRT-PCR were analyzed using the $\Delta\Delta C_t$ method. Two replicates were considered for each of the experimental conditions (aligned fibers with and without electrical stimulation), each one using the RNA harvested from just a single microfluidic device.

2.9. Statistical analysis

All data were statistically analyzed using Prism 8.3 software (GraphPad Software, US). Data were tested for normality and presented and analyzed with mean and standard deviation or median and quartile. Student's t-test (unpaired, two-tailed distribution) was used to compare two samples, while a one-way ANOVA followed by a post hoc Tukey's test was used for multiple samples (unless otherwise specified). A p-value < 0.05 (*) was considered statistically significant.

3. Results and discussion

3.1. Fabrication of microfluidic devices with nanopatterned substrates

Our results show that the electrospinning of nanofibers is an effective way to generate either random or aligned nanotopographies for microfluidic devices, as observed in SEM micrographs (**Fig.2-a,b**). The differences in fiber orientation were quantified by performing an FFT analysis and radial summation of the oval profile of SEM images. A clear peak at 90° can be observed for the aligned fibers (**Fig.2-c**) while a random distribution at different angles is seen for the randomly distributed ones (**Fig.2-d**). A series of different electrospinning parameters were tested till the optimal configuration was found, which yielded continuous and homogenous fiber thicknesses of $1702.3 \pm$

128.9 nm for the random fibers and 697.3 ± 30.9 nm for the aligned ones (**Fig.2-e**) with no bead content. The approached elastic modulus was isotropic for the random nanofibers, with a mean value of 21.1 ± 3.9 MPa, while for the aligned ones the value in the direction of the fibers was 516.5 ± 80.3 MPa (**Fig.2-f**).

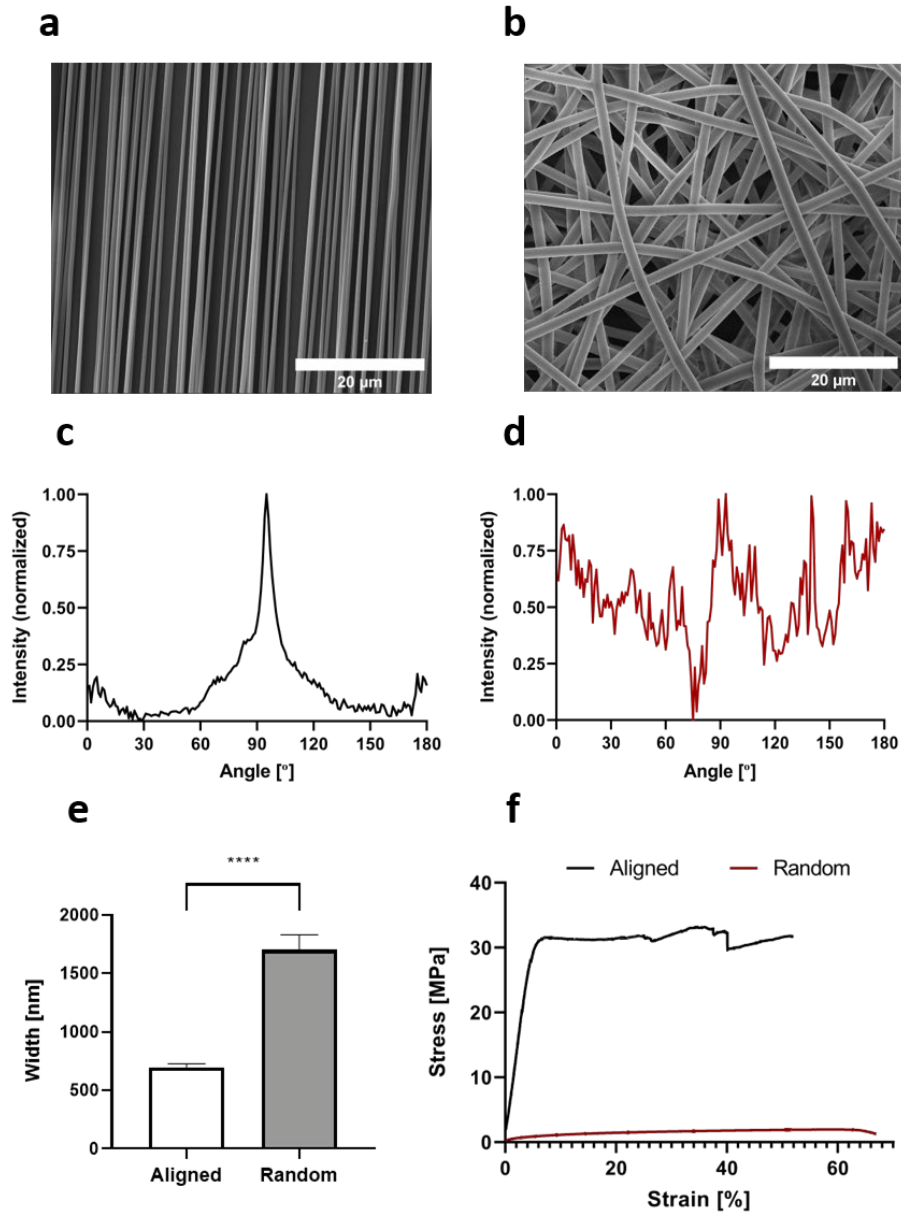


Figure 2 Electrospun fibers characterization. (a,b) Field emission scanning electron microscopy (SEM) images showing the morphology of the aligned and random fibers, respectively. (c,d) FFT analysis of the nanofiber orientation based on the SEM images. (e) Mean nanofiber diameter for each of the conformations. (f) Characteristic stress-strain curves obtained for the tensile mechanical assay of each sample type. Scale bar in (a,b) = 20 μ m. Data in (e) expressed as mean \pm standard deviation ($n = 18$) with **** $p < 0.0001$ (evaluated with Student's t-test).

A robust method to incorporate the electrospun substrates into our microfluidic system was also developed. As the high hydrophobicity of the PLA fibers ($\sim 130^\circ$)⁴⁷ hampers the bonding process of the coverslips to the PDMS devices, we carefully removed most of them from the substrate with a cloth bathed in acetone, leaving only a small rectangle slightly bigger than the cell chamber (around 2 cm wide and 10 cm long). This allowed the PDMS frame to hang on and fix the fibers preventing their detachment from the coverslip when immersed in cell media. The bonding process could be successfully performed for all the experiments and we did not observe any leakage of media during cell culturing within the devices. Another advantage of using PDMS as a frame is its transparency, which together with the fact that we use thin coverslips as substrates (0.17 mm) and low thickness electrospun layers ($\sim 12 \mu\text{m}$), makes our device compatible with high-resolution imaging platforms such as confocal microscopes.

Overall, we consider electrospinning to be a much more robust, reproducible, cost-effective, and scalable approach to generate nanopatterned substrates for microfluidic chips than previously presented methods such as microcontact printing¹³⁻¹⁵, hydrogel patterning with microfluidic channels^{16,17}, or hot embossing¹⁹. It is a single-step procedure performed with commonly used equipment (such as pumps, or a high voltage source) while previously used techniques are multistep and require expensive microfabricated molds generally obtained through photolithography. It also offers high versatility, as it is possible to easily customize many different fabrication parameters such as fiber orientation, thickness, length, positioning density or type of polymer material (natural, synthetic or blended)^{21,23,48}. In our case, we chose PLA 70/30 due to its excellent biocompatibility and cell adhesion properties observed in previous works from our group^{49,50}. The mechanical strength and chemical stability of this material make it compatible with procedures such as plasma bonding or UV light sterilization, which is an important limitation of the techniques that rely on natural polymers such as collagen, which tend to collapse due to their low ultimate strength and undergo degradation when exposed to UV light⁵¹. Finally, our device can also be easily customized to incorporate

perfusion by changing the size of the reservoirs and connecting it to a pumping system by using the appropriate tubing. This is something that cannot be easily addressed in most of the previously presented methods, which generally rely on systems placed inside well-plates or Petri dishes^{18,19,29,38}, in which incorporating perfusion is not even an option. Despite all the experiments were carried out in static conditions, a computational simulation of the flow pattern (see **Fig.S1**) was performed to assess the shear stress cardiac cells would be subjected to in the case of incorporating a perfusion system (more details in **Supplementary Methods**). The estimated stress in the cell chamber was 0.04 dyn cm⁻² (for a flow of 100 μ l h⁻¹), which is orders of magnitude lower than even the shear stress needed to start inducing cell alignment (3 dyn cm⁻²)⁵². This means that the seeded cells would be minimally affected in the case flow was incorporated.

3.2. Electrical stimulation model of the microfluidic system

The development of a reliable electrical model of our platform is essential in order to demonstrate that our approach can generate the required conditions to optimally stimulate cardiac cells. It is generally considered that a uniform electrical field of 5 V/cm, 2 ms in duration, and 1 Hz in frequency can mimic the characteristics of the electrical impulses in murine native myocardium²⁹. After performing some preliminary testing, we found that placing the electrodes tangent to the media channels and aligned with cell chamber inlets yields the best trade-off between design simplicity and maximizing the electrical field strength in the cell chamber. Then, we evaluated the possibility of performing the stimulation using just two rod-shaped electrodes at each end of the chamber. Unfortunately, we found that this was not a suitable approach, as the generated field was not homogeneous because the x-components (corresponding to cell chamber width direction) did not cancel each other (see **Fig.S2-a**).

To solve this problem, we introduced two extra electrodes placed symmetrically at each end of the chamber (see **Fig.3-a**), which proved to completely remove the x-component (see **Fig.3-b**). This makes the field to be completely homogenous in the

length direction (y -component) for most of the cell chamber, with the logical perturbations around the PDMS posts structures due to the insulator properties of this polymer. This is further confirmed by observing the field lines (**Fig.3-c**), which show that the current flow goes completely in the electrode-electrode direction (matching also with the alignment of the electrospun fibers). This is an important point, as it has been shown that cardiomyocytes are more excitable when their long axis is parallel to the electrical field lines^{29,53}, so the electrical field should ideally go in the same direction as the contact cues. Another interesting point is that the required input voltage to generate a field of around 5 V/cm is significantly lower in the case of the four-electrode configuration (around 5 V) than in the two-electrode one (around 8 V). In both cases, we observed that the z -component is zero, which means that the homogeneity is maintained for all the height of the chamber.

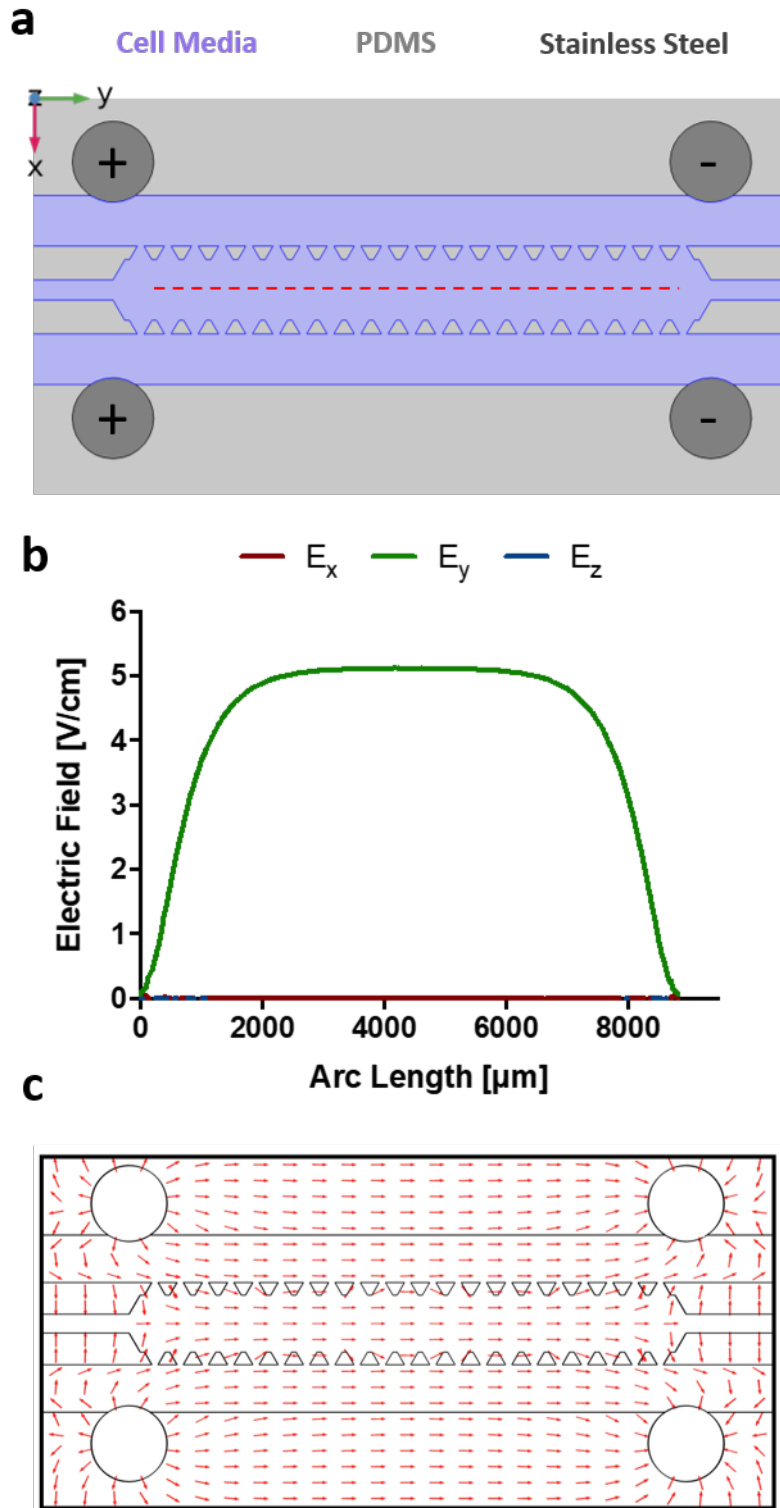


Figure 3 Electrical finite element model results. **(a)** Layout and materials composing the different parts of the system: cell chamber filled with culture media, PDMS frame and posts, and four stainless-steel electrodes. The red line indicates the section across which the electrical field was computed ($z = 75 \mu\text{m}$). **(b)** Electrical field intensity corresponding to the transversal section previously indicated decomposed in its different components (x,y,z) for an input voltage of $5 V_{pp}$. **(c)** Electrical field vectors in a cross-section of the cell chamber ($z = 75 \mu\text{m}$), indicative of the direction of current flow.

Regarding the validity of the simulations, we have to consider that they are performed under steady-state conditions. Any bioreactor using solid electrodes to apply electrical stimulation has a dynamic electrical behavior that derives from the way the charge is transduced into the electrolyte (generally cell media). This process occurs via reversible and non-reversible faradaic reactions and the non-faradaic charging/discharging of the double layer formed in the electrode/electrolyte interface ³¹. In our case, we consider the steady-state conditions as an electroquasistatic approximation of the dynamic electrical behavior of the system, which gives us detailed spatial information rather than a description of the time evolution of the system. This is a valid assumption when considering homogenous, isotropic media, and wavelengths under 10 kHz ^{30 38}., all of which are fulfilled in our experiment.

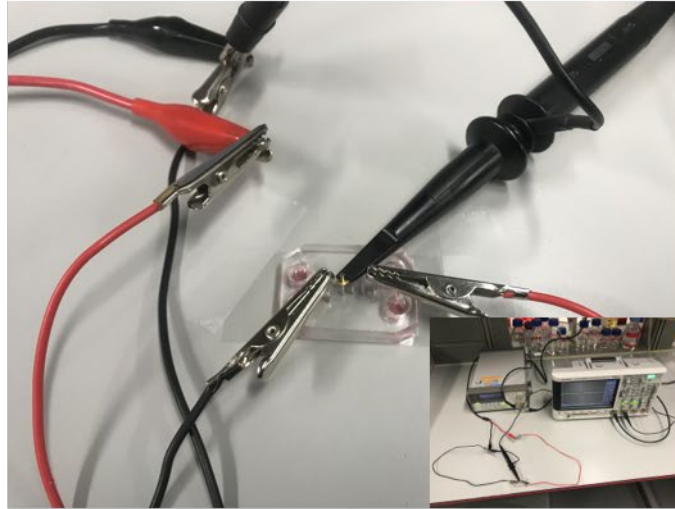
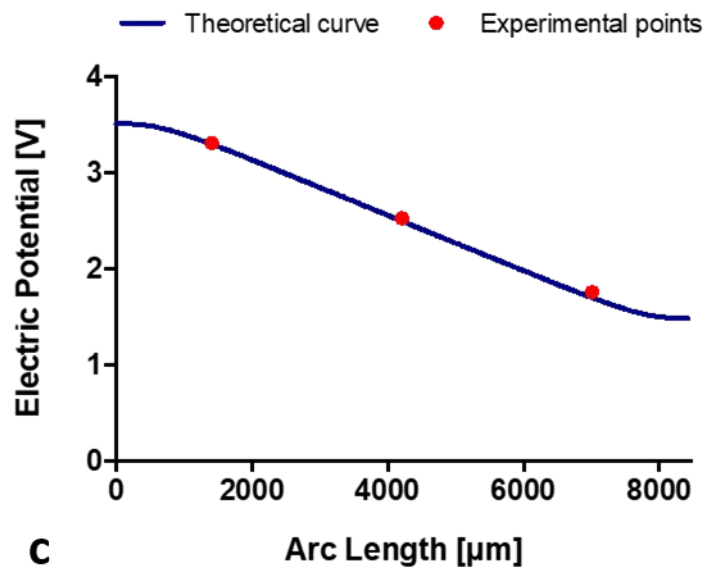
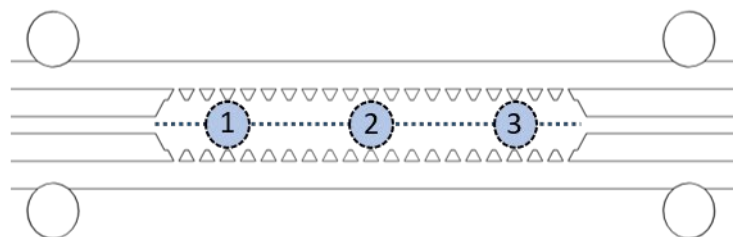
a**b****c**

Figure 4 Electrical characterization of the device. (a) The used experimental setup to perform the voltage measurements. (b) Comparison of the theoretical curve obtained in the simulations of the electrical potential with respect to the experimental voltage measurements (red dots). (c) Schematic of the device showing the section for which the electric potential was calculated in the simulations ($z = 75$) and the three holes performed in the cell chamber of the device to obtain the experimental measurements. Experimental data in (b) expressed as mean \pm standard deviation ($n = 3$). Note

that the error bars cannot be seen because of the really small deviations: ± 0.03 V for points number 1,2 and ± 0.02 for point number 3.

To make sure that the developed electrical model is able to predict the actual electrical field distribution in our device, we compared the theoretical voltage curve obtained in the simulations with experimental measurements performed in three different positions inside the cell chamber (see **Fig.4-a,c**). The pulse characteristics were the same as in the cell stimulation protocol: biphasic wave with an amplitude of $5 V_{pp}$, 2 ms in duration, and 1 Hz in frequency. We evidenced that the experimental measurements perfectly matched the theoretical curves with minimal differences between devices (see **Fig.4-b**, the three independent microfluidic chips). For the first position (approximately $1408 \mu\text{m}$ from the start of the cell chamber) we measured a value of 3.31 ± 0.03 V, which is close to the 3.28 V estimated in the finite element simulation. For the second and third positions ($4208 \mu\text{m}$ and $7008 \mu\text{m}$ respectively from the chamber inlet) we obtained values of 2.55 ± 0.03 V and 1.77 ± 0.02 V which also matched the estimated simulation values of 2.52 V and 1.72 V.

3.3. Comparison of the developed system to “gold standard” planar electrodes

The use of rod-shaped carbon electrodes is the most common approach to stimulate cardiac cells in macroscale platforms, due to their excellent properties in terms of biocompatibility and injected charge (95 % of charge is transduced into the bioreactor during the stimulus pulse)³⁰. However, they cannot be easily integrated into microfluidic platforms because of their poor mechanical properties. The most common approach to stimulate this type of cell in microsize devices is the deposition of planar microelectrodes on fixed positions of the substrate^{19,38}. Since this approach is considered the gold standard, we compared our system to an equivalent version in which planar electrodes were used. To that end, we performed a simulation considering the patterning of two rectangular gold electrodes ($120 \mu\text{m}$ in width and 800 nm in height based on the parameters from a previously proposed system¹⁹) in the same position as the rod-shaped stainless-steel ones (aligned with the cell chamber inlets).

The results of the simulation (supplementary **Fig.S2-b**) show that the planar electrodes require just a slightly lower input voltage (around 4.6 V) to generate the 5 V/cm field compared to the four-electrode configuration (~5 V). Another difference is that the field is completely homogenous for all the chamber's length, while in the 4-electrode configuration there is a slope to reach and drop from the 5 V/cm value for approximately the first and last millimeter of the chamber. However, the use of planar electrodes has many limitations: its microfabrication is generally a complex procedure requiring expensive equipment (such as photolithography mask aligners or evaporators) and materials (gold, platinum, etc.) with the resulting devices being generally not reusable due to the irreversible nature of the bonding process. Moreover, their planar nature may not ensure the uniformity of the electrical field throughout the different heights³⁷, which is critical in case a 3D culture is performed.

3.4. Generation of highly anisotropic cardiac tissue with improved maturation.

Cardiac cells were seeded on our MPS to evaluate tissue alignment and maturation after 7 days in culture (5 of which under electrical stimulation). In the case of the randomly deposited fibers, the distribution of the cardiomyocyte contractile proteins was completely isotropic, showing no preferential angle of orientation (**Fig.5-a,c**), while in the case of the aligned ones, the cells are polarized in the direction of the nanofibers (0°) with a small deviation of $\pm 5^\circ$ (**Fig.5-b,c**). Cells were also clearly more elongated in the aligned fibers, acquiring a fusiform shape that closely mimics the morphology of cardiomyocytes found in native myocardium⁵⁴. From the electrospinning variables, the used fiber density is probably the main regulator of the resulting tissue architecture, as it drives two processes: the first step during cell seeding and attachment, in which the fibers provide contact guidance, and the second step of intercellular guidance caused by the growth and close interaction of neighboring cells²¹. High fiber densities are recommended to obtain optimal ordering, co-alignment, and elongation of cardiac cells, so we made sure to completely fulfill this requirement by depositing around 1160

fibers/mm. This is also beneficial in terms of generating a nanoscale topography with a high specific surface area, which is essential for optimal cell attachment and growth ²³.

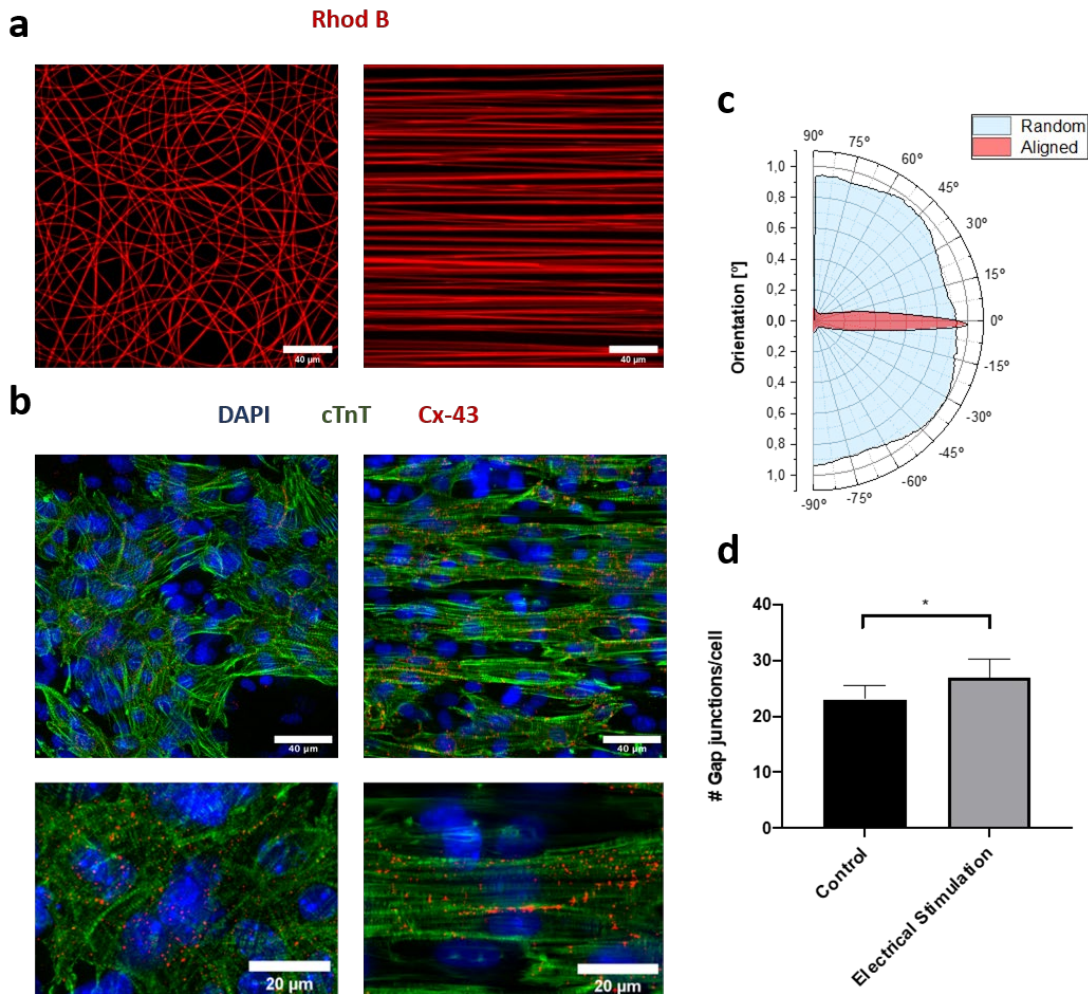


Figure 5 Immunofluorescence staining of the cardiac tissue and quantification of orientation and gap junctional proteins expression. **(a)** Fluorescent microscope images of the random electrospun fibers containing rhodamine B (red) and the cardiomyocytes seeded on top stained for the contractile protein troponin T (green), gap junctional protein connexin-43 (red), and cell nuclei (blue) after 7 days in regular culture. **(b)** Fluorescent microscope images of the aligned electrospun fibers containing rhodamine B (red) and the cardiomyocytes seeded on top stained for the contractile protein troponin T (green), gap junctional protein connexin-43 (red), and cell nuclei (blue) after 7 days in culture (5 of them with electrical stimulation). Scale bar in (a,b) = 40 μm (20 μm in magnification view). **(c)** Polar plot of the differences in the orientation between the cardiomyocytes seeded on top of the aligned vs random electrospun substrates. Results represent the normalized mean values distribution ($n = 6$) for different angles between -90° to 90° . **(d)** Analysis of the number of measured Cx-43 gap junctional protein (Cx-43) dots per cell. Results are expressed as mean \pm standard deviation ($n = 6$) with $*p < 0.05$ (evaluated with Student's t-test).

Cardiomyocytes formed confluent cell monolayers capable of spontaneously contracting on top of the nanofibers (see **Supplementary Movie 1**). This is in line with

previous studies that show that thin meshes provide contact guidance and oriented growth to the cells while still allowing some degree of cellular contraction ²¹. Compared to previously presented microsystems, which are generally based on the microfabrication of geometries not naturally occurring *in vivo*, such as rectangular lanes made of different materials ^{13,16,17,19}, nanofibrous scaffolds have the advantage of providing a much more physiologically relevant environment for cardiac cells as they closely resemble the native fibrous network of the extracellular matrix of the heart ⁸. One important consideration is that the stiffness of the PLA fibers is several orders of magnitude higher than the physiological range for neonatal mice ⁵⁵ (around 4-11.4 kPa) or human ⁹ (10-500 kPa) myocardium, which has been shown to increase cardiac fibroblasts proliferation ⁵⁵. An overgrowth of fibroblasts may compromise the generation of a confluent contractile monolayer due to the limited proliferative capacity of the cardiomyocytes. Therefore, during the isolation procedure, we made sure that the cardiac cell population was highly enriched in cardiomyocytes, and cells were seeded at high densities (20×10^6 cells/ml). The complete removal of fibroblasts, however, is not recommended, as their presence has been demonstrated to significantly improve the morphological and functional properties of the resulting cardiac constructs ^{56,57}.

High stiffness substrates have also been widely acknowledged to promote fibroblast activation by integrin-mediated mechanotransduction pathways, leading to the development of ultrastructural and phenotypic characteristics of smooth muscle cells ^{58,59}. Myofibroblasts have a contractile apparatus formed by stress fibers (actin myofilaments) and associated contractile proteins, used to exert traction forces and migrate ⁶⁰. One of the characteristic contractile proteins expressed by myofibroblasts is the non-muscle myosin heavy chain B (SMemb) ⁶¹. We compared the expression of this protein in PLA substrates with respect to compliant polyacrylamide gels (30 kPa), which are within the physiological stiffness of neonatal mice and human myocardium. Our results (see **Fig.S3**) clearly show a higher expression of the SMemb protein in the case of the PLA substrates, which confirms that their high stiffness is driving myofibroblast

activation. These cells tend to form nanotube attachments to cardiac myocytes and may thus act as capacitors in our co-culture system.

As previously described, we also incorporated electrical stimulation into our system. We selected AISI 304 stainless steel electrodes due to their excellent biocompatibility, mechanical properties, and charge transfer characteristics from the electrode to the cell media (75 % of injected charge)³⁰. One common concern about the use of these electrodes is that they are more susceptible to faradaic reactions than carbon electrodes because they leave a higher amount of unrecovered electrical charge, which makes them more likely to undergo corrosion and generate harmful byproducts⁶². However, this can be easily minimized using an adequate stimulation protocol. First, short pulses (2 ms in duration) are enough to excite cardiac cells while sufficiently short to dissipate double layer effects on the electrodes between subsequent pulses³¹. Additionally, the use of biphasic waves is an effective way to balance the charge and counteract the irreversible reactions happening at the interface of the electrodes and culture medium, which leads to an accumulation of charge with undesirable side-effects (electrolysis, pH gradients, etc.)⁶³. We successfully implemented this approach in our platform, as we did not observe any bubble formation at the electrode sites or changes in the color of the phenol red present in the medium during the time of culture. Moreover, with the daily change of media, we made sure that we eliminated any potential accumulation of byproducts that may have formed during the stimulation.

As previously commented, cardiomyocytes tend to align parallel to the direction of the electrical field lines^{29,53}, while the fibroblasts strongly orient perpendicularly to the field lines, especially when DC is used^{18,64}. However, previous studies have shown that the use of topographical cues saturates the cellular signaling pathways leading to cellular orientation^{18,19}. As a result, the use of electrical stimulation would fail to promote further cellular elongation. Therefore, the main goal of incorporating electrical cues in our platform is to enhance the development of conductive and contractile properties of the

cardiac constructs. This is an important feature, as it has been shown that electrospun fibers alone have a limited effect on cardiomyocyte maturation ⁶⁵. One of the most important points in this regard is the development of cardiac gap junctions, which are transmembrane intercellular channels that enable the propagation of electrical signals across the cardiac tissue and, subsequently, the activation and development of the contractile apparatus ⁶. Immunofluorescence analyses show a moderate but significant increase for connexin-43 (Cx-43, the major cardiac gap junctional protein in heart tissue) in the stimulated tissues compared to the controls (**Fig.5-d**). Interestingly, their distribution also shows a clear trend from being randomly dispersed in the cytosol in the case of the unstimulated controls (**Fig.5-a**) to a progressive localization in the membrane border of the elongated cells in the stimulated ones (**Fig.5-b**), which is widely considered to be their functional location in adult cardiomyocytes ⁶⁶.

Several factors were taken into account to achieve an enhanced expression and localization of this protein. First, it has been evidenced that the optimal time to start the electrical stimulation is between 1-3 days after cell seeding ³¹. If applied too early, cells will not have time to recover from the isolation process, and the production and reassembling of conductive proteins will be inhibited, leading to poor contractile behavior. On the other hand, if applied too late the effects of the stimulation will be minimal due to the reduced amount of contractile properties available in the cells ²⁹. Additionally, the use of biphasic pulses has been shown to yield better functional and structural properties in cardiac constructs compared to monophasic pulses ⁶⁷. This is attributed to the synergistic effect of the two phases of the pulses, with the first one acting as conditioning subthreshold prepulse and the second phase as an excitatory pulse ⁶⁸.

We further studied the effects of our electrical stimulation setup in driving cell maturation by analyzing the transcriptional expression of several key cardiac markers. On the one hand, we focused on the development of functional gap junctions and cell-to-cell coupling by analyzing the GJA1 gene, which encodes the connexin-43 protein.

We observed a 2.5-fold increase in the expression of this gene in the electrically stimulated samples compared to the unstimulated controls (**Fig.6-a**), which closely agrees with the Cx-43 expressed at the protein level and supports the idea that electrical stimulation is the main factor enhancing cell maturation. We also evaluated the development of the contractile apparatus by quantifying the TNNI3 gene, which encodes cardiac troponin I, a key component of the actin-based thin filaments. Interestingly, we found a 7-fold increase in the expression of this gene compared to the unstimulated samples (**Fig.6-b**). This result suggests a higher degree of maturation, as this isoform of the troponin is often associated with an adult phenotype⁶. The values obtained for both the TNNI3 and GJA1 are in the range reported for macroscale bioreactors⁶⁹, showing the capabilities of our miniaturized system in achieving similar degrees of maturation to much more complex and costly setups.

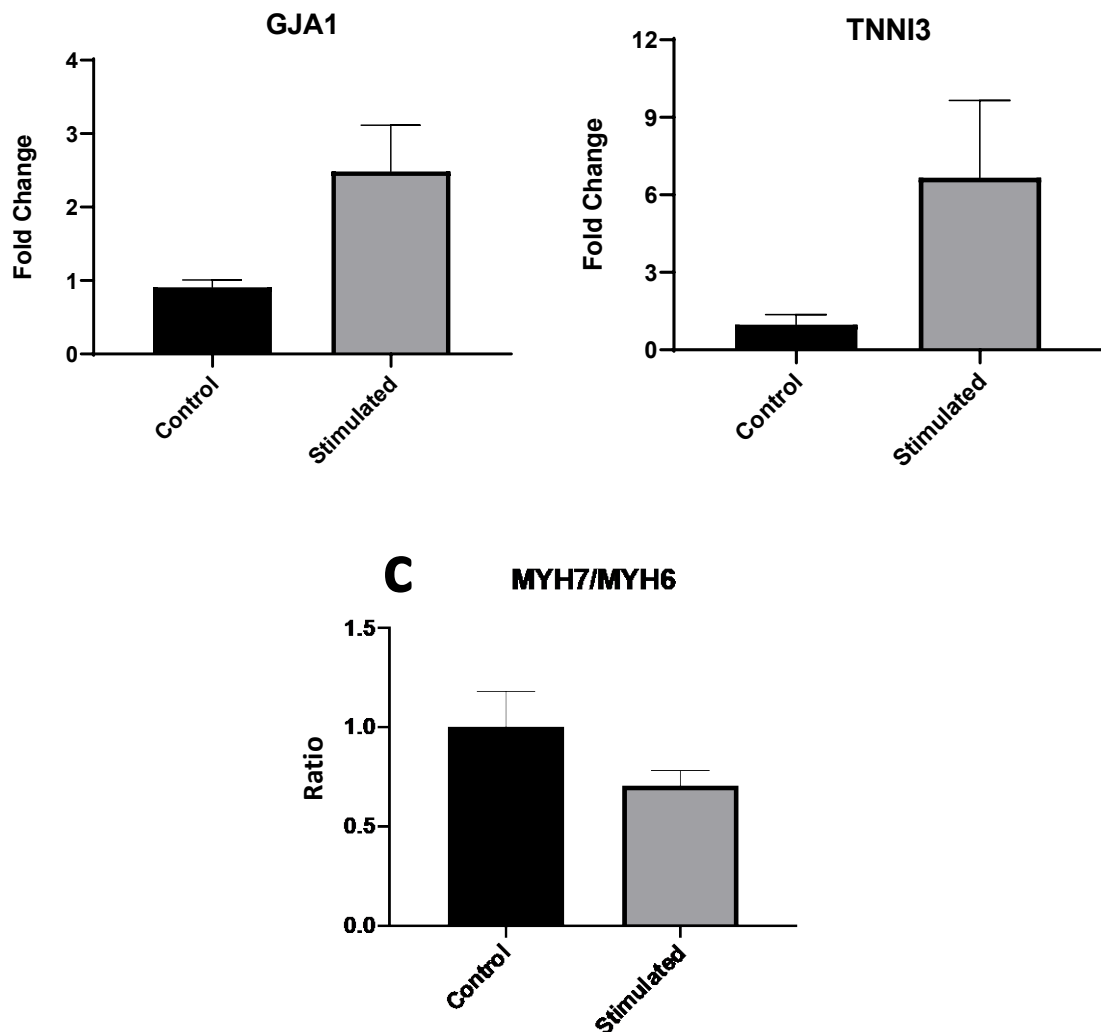


Figure 6 RT-qPCR analysis of the transcriptional expression of different cardiac markers: (a) Connexin-43 (encoded by GJA1 gene), (b) Troponin I (encoded by TNNI3 gene) and (c) ratio between myosin heavy chain alpha and beta isoforms (encoded by the MYH7 and MYH6 genes respectively). Gene expression values are computed as fold changes using the ΔC_t method and expressed as a ratio concerning the control condition. Results are expressed as mean \pm standard deviation ($n = 2$) with $*p < 0.05$ (evaluated with Student's t-test).

We also evaluated MYH6 and MYH7 genes, which respectively encode the α -(fast) and β - (slow) heavy chain subunits of the cardiac myosin. The β -subunit is associated with a more adult-like phenotype, while the α -subunit tends to be higher in a fetal stage⁷⁰. Therefore, it is important to quantify the β -MHC/ α -MHC ratio, as it increases with the developmental stage⁶. We found lower levels in the expression of MYH7 concerning MYH6 in electrically stimulated samples compared to controls (**Fig.6-c**). We believe

that this fact is derived from the limitations of the 2D configuration, as these proteins are more dependent on mechanotransduction pathways than troponin for their development^{71,72}. In 2D setups, the use of high stiffness substrates prevents the same level of contraction and remodeling as in highly compliant 3D scaffolds, which leads to some degree of degradation and decrease in the synthesis of sarcomeric proteins⁷³.

4. Conclusions

In this study, we present a microfluidic cell culture system able to generate a highly biomimetic 2D cardiac tissue by incorporating topographical and electrical cues more simply and efficiently than previously reported platforms, representing a useful tool for the tissue engineering community. We describe a method to generate electrospun-coated substrates in closed microdevices and validate its potential to consistently yield highly anisotropic cardiac microtissues. Moreover, we describe a simple and cost-effective strategy to place electrodes in a microfluidic system. An experimentally validated finite element model of our device shows that this approach is able to generate electrical fields with a magnitude comparable to the golden standard based on planar electrodes with similar input voltages. The functionality of the electrical setup for the maturation of the cardiac constructs is also evidenced by the upregulation of key cardiac genes related to the contractile apparatus (troponin I) and conductive properties (upregulation of tight junctional protein Cx-43 at both gene and protein level). Nevertheless, some limitations related to the high stiffness of the 2D substrate are also observed, which leads to a slight decrease in the ratio of β -MHC/ α -MHC ratio, often related to a more immature phenotype. Further work is therefore required to address this issue by implementing more compliant substrates that allow a higher degree of remodeling.

ASSOCIATED SUPPLEMENTARY MATERIAL

The associated supplementary material contains the methodology used to create the computational finite element model of the flow pattern in our device, estimate the resulting shear stress in the cell chamber, and the evaluation of cardiac fibroblast activation by immunostaining. Supplementary figures are also provided showing the results obtained for the flow simulation, immunostaining images of the cardiac fibroblasts, and the simulation results for alternative electrical stimulation approaches. Finally, a supplementary video showing cardiomyocytes beating on top of the PLA nanofibers is also included.

AUTHOR INFORMATION

Corresponding Author

*e-mail: oscar.castano@ub.edu

DISCLOSURE

The authors declare no competing financial interest.

ACKNOWLEDGEMENTS

The authors would like to thank Dra. Elena Rebollo Arredondo from the Molecular Imaging Platform of the Molecular Biology Institute of Barcelona (IBMB) for her advice and training on microscopy, David Izquierdo Garcia from the MicroFabSpace of the Institute for Bioengineering of Catalonia (IBEC) for his advice and training in microfabrication, Gerard Rubí Sans from the Biomaterials for Regenerative Therapies Group at IBEC for offering his expertise on polyacrylamide gels, and Adrianna Glinkowska Mares from the Nanoscopy for Nanomedicine at IBEC for her availability and valuable advice on microfluidics.

FUNDING

This work has been funded with the support of the European Regional Development Fund (FEDER) and Spanish Ministry of Science and Innovation (MICINN) with the projects MICINN (BES-2015-071997, MAT2015-62725-ERC, RTI2018-096320-B-C21, RTI2018-097038-B-C21, and RTI2018-097038-B-C22), the European Commission-Euronanomed nAngioderm project (JTC2018-103) and the Spanish network of cell therapy (TERCEL) for financial support. Finally, researchers also thank Programme/Generalitat de Catalunya (2017-SGR-359) and the Severo Ochoa programme of the Spanish Ministry of Science and Innovation (MICINN - Grant SEV-2014-0425, 2015-2019 and CEX2018-000789-S, 2019-2023). A.L.C. thanks MICINN for FPU fellowship FPU17/06161.

5. References

- ¹ G.C. Engelmayr, M. Cheng, C.J. Bettinger, J.T. Borenstein, R. Langer, and L.E. Freed, *Nat. Mater.* **7**, 1003 (2008).
- ² L.L.Y. Chiu and M. Radisic, *Curr. Opin. Chem. Eng.* **2**, 41 (2013).
- ³ R.L. Carrier, M. Papadaki, M. Rupnick, F.J. Schoen, N. Bursac, R. Langer, L.E. Freed, and G. Vunjak-Novakovic, *Biotechnol. Bioeng.* **64**, 580 (1999).
- ⁴ S.N. Bhatia and D.E. Ingber, *Nat. Biotechnol.* **32**, 760 (2014).
- ⁵ E.W. Esch, A. Bahinski, and D. Huh, *Nat. Rev. Drug Discov.* **14**, 248 (2015).
- ⁶ N.T. Feric and M. Radisic, *Adv Drug Deliv Rev* **96**, 110 (2016).
- ⁷ B. Liao, N. Christoforou, K.W. Leong, and N. Bursac, *Biomaterials* **32**, 9180 (2011).
- ⁸ C.W. Hsiao, M.Y. Bai, Y. Chang, M.F. Chung, T.Y. Lee, C.T. Wu, B. Maiti, Z.X. Liao, R.K. Li, and H.W. Sung, *Biomaterials* **34**, 1063 (2013).

- ⁹ Y. Zhao, N. Rafatian, N.T. Feric, B.J. Cox, R. Aschar-Sobbi, E.Y. Wang, P. Aggarwal, B. Zhang, G. Conant, K. Ronaldson-Bouchard, A. Pahnke, S. Protze, J.H. Lee, L. Davenport Huyer, D. Jekic, A. Wickeler, H.E. Naguib, G.M. Keller, G. Vunjak-Novakovic, U. Broeckel, P.H. Backx, and M. Radisic, *Cell* **176**, 913 (2019).
- ¹⁰ N. Thavandiran, S.S. Nunes, Y. Xiao, and M. Radisic, *Stem Cell Res. Ther.* **4**, 1 (2013).
- ¹¹ J.L. Wilbur, A. Kumar, E. Kim, and G.M. Whitesides, *Adv. Mater.* **6**, 600 (1994).
- ¹² Y. Xia and G.M. Whitesides, *Annu. Rev. Mater. Sci.* **28**, 153 (1998).
- ¹³ N. Bursac, K.K. Parker, S. Iravanian, and L. Tung, *Circ. Res.* **91**, (2002).
- ¹⁴ A.W. Feinberg, P.W. Alford, H. Jin, C.M. Ripplinger, A.A. Werdich, S.P. Sheehy, A. Grosberg, and K.K. Parker, *Biomaterials* **33**, 5732 (2012).
- ¹⁵ N. Badie, L. Satterwhite, and N. Bursac, *Ann. Biomed. Eng.* **37**, 2510 (2009).
- ¹⁶ A. Khademhosseini, G. Eng, J. Yeh, P.A. Kucharczyk, R. Langer, G. Vunjak-Novakovic, and M. Radisic, *Biomed. Microdevices* **9**, 149 (2007).
- ¹⁷ J.M. Karp, Y. Yeo, W. Geng, C. Cannizarro, K. Yan, D.S. Kohane, G. Vunjak-Novakovic, R.S. Langer, and M. Radisic, *Biomaterials* **27**, 4755 (2006).
- ¹⁸ H.T.H. Au, I. Cheng, M.F. Chowdhury, and M. Radisic, *Biomaterials* **28**, 4277 (2007).
- ¹⁹ H.T. Heidi Au, B. Cui, Z.E. Chu, T. Veres, and M. Radisic, *Lab Chip* **9**, 564 (2009).
- ²⁰ S.A. Sell, M.J. McClure, K. Garg, P.S. Wolfe, and G.L. Bowlin, *Adv. Drug Deliv. Rev.* **61**, 1007 (2009).
- ²¹ Y. Orlova, N. Magome, L. Liu, Y. Chen, and K. Agladze, *Biomaterials* **32**, 5615 (2011).
- ²² P. Joanne, M. Kitsara, S.E. Boitard, H. Naemetalla, V. Vanneaux, M. Pernot, J. Larghero, P. Forest, Y. Chen, P. Menasché, and O. Agbulut, *Biomaterials* **80**, 157 (2016).
- ²³ X. Zong, H. Bien, C.Y. Chung, L. Yin, D. Fang, B.S. Hsiao, B. Chu, and E. Entcheva,

Biomaterials **26**, 5330 (2005).

²⁴ Y.D. Lin, M.C. Ko, S.T. Wu, S.F. Li, J.F. Hu, Y.J. Lai, H.I.C. Harn, I.C. Laio, M.L. Yeh, H.I. Yeh, M.J. Tang, K.C. Chang, F.C. Su, E.I.H. Wei, S.T. Lee, J.H. Chen, A.S. Hoffman, W.T. Wu, and P.C.H. Hsieh, *Biomater. Sci.* **2**, 567 (2014).

²⁵ E.J. Suuronen and M. Ruel, *Biomaterials for Cardiac Regeneration* (2015).

²⁶ N.L. Tulloch, V. Muskheli, M. V. Razumova, F.S. Korte, M. Regnier, K.D. Hauch, L. Pabon, H. Reinecke, and C.E. Murry, *Circ. Res.* **109**, 47 (2011).

²⁷ G.S. Ugolini, R. Visone, D. Cruz-Moreira, A. Mainardi, and M. Rasponi, *Methods Cell Biol.* **146**, 69 (2018).

²⁸ H. Parsa, B.Z. Wang, and G. Vunjak-Novakovic, *Lab Chip* **17**, 3264 (2017).

²⁹ M. Radisic, H. Park, H. Shing, T. Consi, F.J. Schoen, R. Langer, L.E. Freed, and G. Vunjak-Novakovic, *Proc. Natl. Acad. Sci. U. S. A.* **101**, 18129 (2004).

³⁰ N. Tandon, A. Marsano, R. Maidhof, L. Wan, H. Park, and G. Vunjak-Novakovic, *J. Tissue Eng. Regen. Med.* **5**, e115 (2011).

³¹ N. Tandon, C. Cannizzaro, P.H.G. Chao, R. Maidhof, A. Marsano, H.T.H. Au, M. Radisic, and G. Vunjak-Novakovic, *Nat. Protoc.* **4**, 155 (2009).

³² M. Valls-Margarit, O. Iglesias-García, C. Di Guglielmo, L. Sarlabous, K. Tadevosyan, R. Paoli, J. Comelles, D. Blanco-Almazán, S. Jiménez-Delgado, O. Castillo-Fernández, J. Samitier, R. Jané, E. Martínez, and Á. Raya, *Stem Cell Reports* **13**, 207 (2019).

³³ R. Maidhof, N. Tandon, E.J. Lee, J. Luo, Y. Duan, K. Yeager, E. Konofagou, and G. Vunjak-Novakovic, *J. Tissue Eng. Regen. Med.* **6**, (2012).

³⁴ Y. Barash, T. Dvir, P. Tandeitnik, E. Ruvinov, H. Guterman, and S. Cohen, *Tissue Eng. - Part C Methods* **16**, 1417 (2010).

³⁵ G. Kensah, I. Gruh, J. Viering, H. Schumann, J. Dahlmann, H. Meyer, D. Skvorc, A.

Bär, P. Akhyari, A. Heisterkamp, A. Haverich, and U. Martin, *Tissue Eng. - Part C Methods* **17**, 463 (2011).

³⁶ I.-C. Liao, J.B. Liu, N. Bursac, and K.W. Leong, *Cell. Mol. Bioeng.* **1**, 133 (2008).

³⁷ R. Visone, G. Talò, P. Occhetta, D. Cruz-Moreira, S. Lopa, O.A. Pappalardo, A. Redaelli, M. Moretti, and M. Rasponi, *APL Bioeng.* **2**, 046102 (2018).

³⁸ N. Tandon, A. Marsano, R. Maidhof, K. Numata, C. Montouri-Sorrentino, C. Cannizzaro, J. Voldman, and G. Vunjak-Novakovic, *Lab Chip* **10**, 692 (2010).

³⁹ A. Pavesi, G. Adriani, M. Rasponi, I.K. Zervantonakis, G.B. Fiore, and R.D. Kamm, *Sci. Rep.* **5**, (2015).

⁴⁰ C.A. Schneider, W.S. Rasband, and K.W. Eliceiri, *Nat. Methods* **9**, 671 (2012).

⁴¹ N. Sachot, O. Castaño, H. Oliveira, J. Martí-Muñoz, A. Roguska, J. Amedee, M. Lewandowska, J.A. Planell, and E. Engel, *J. Mater. Chem. B* **4**, (2016).

⁴² Z. Alvarez, M.A. Mateos-Timoneda, P. Hyrossova, O. Castano, J.A. Planell, J.C. Perales, E. Engel, and S. Alcantara, *Biomaterials* **34**, 2221 (2013).

⁴³ N. Sachot, M.A. Mateos-Timoneda, J.A. Planell, A.H. Velders, M. Lewandowska, E. Engel, and O. Castaño, *Nanoscale* **7**, 15349 (2015).

⁴⁴ J. Ordoño, S. Pérez-Amodio, K. Ball, A. Aguirre, and E. Engel, *BioRxiv* 2020.07.21.213736 (2020).

⁴⁵ J. Schindelin, I. Arganda-Carreras, E. Frise, V. Kaynig, M. Longair, T. Pietzsch, A. Preibisch, C. Rueden, S. Saalfeld, B. Schmid, J.Y. Tinevez, D.J. White, V. Hartenstein, K. Eliceiri, P. Tomancak, and A. Cardona, *Nat. Methods* **9**, 676 (2012).

⁴⁶ Z. Püspöki, M. Storath, D. Sage, and M. Unser, *Adv. Anat. Embryol. Cell Biol.* **219**, 69 (2016).

⁴⁷ Z. Álvarez, O. Castaño, A. a. Castells, M. a. Mateos-Timoneda, J. a. Planell, E. Engel,

and S. Alcántara, *Biomaterials* **35**, 4769 (2014).

⁴⁸ N. Sachot, O. Castano, J.A. Planell, and E. Engel, *J. Biomed. Mater. Res. - Part B Appl. Biomater.* **103**, (2015).

⁴⁹ Z. Álvarez, M. a Mateos-Timoneda, P. Hyroššová, O. Castaño, J. a Planell, J.C. Perales, E. Engel, and S. Alcántara, *Biomaterials* **34**, 2221 (2013).

⁵⁰ H. Oliveira, S. Catros, C. Boiziau, R. Siadous, J. Marti-Munoz, R. Bareille, S. Rey, O. Castano, J. Planell, J. Amédée, and E. Engel, *Acta Biomater.* **29**, 435 (2016).

⁵¹ K. Jariashvili, B. Madhan, B. Brodsky, A. Kuchava, L. Namicheishvili, and N. Metreveli, *Biopolymers* **97**, 189 (2012).

⁵² C. Wang, H. Lu, and M. Alexander Schwartz, *J. Biomech.* **45**, 1212 (2012).

⁵³ L. Tung, N. Sliz, and M.R. Mulligan, *Circ. Res.* **69**, 722 (1991).

⁵⁴ Y. Xiao, B. Zhang, H. Liu, J.W. Miklas, M. Gagliardi, A. Pahnke, N. Thavandiran, Y. Sun, C. Simmons, G. Keller, and M. Radisic, *Lab Chip* **14**, 869 (2014).

⁵⁵ B. Bhana, R.K. Iyer, W.L.K. Chen, R. Zhao, K.L. Sider, M. Likhitpanichkul, C.A. Simmons, and M. Radisic, *Biotechnol. Bioeng.* **105**, 1148 (2010).

⁵⁶ M. Radisic, H. Park, T.P. Martens, J.E. Salazar-Lazaro, W. Geng, Y. Wang, R. Langer, L.E. Freed, and G. Vunjak-Novakovic, *J. Biomed. Mater. Res. - Part A* **86**, 713 (2008).

⁵⁷ H. Naito, I. Melnychenko, M. Didié, K. Schneiderbanger, P. Schubert, S. Rosenkranz, T. Eschenhagen, and W.H. Zimmermann, *Circulation* **114**, (2006).

⁵⁸ J. Solon, I. Levental, K. Sengupta, P.C. Georges, and P.A. Janmey, *Biophys. J.* **93**, 4453 (2007).

⁵⁹ P. Pakshir, N. Noskovicova, M. Lodyga, D.O. Son, R. Schuster, A. Goodwin, H. Karvonen, and B. Hinz, *J. Cell Sci.* **133**, (2020).

⁶⁰ C. Steenbergen and N.G. Frangogiannis, in *Muscle* (Elsevier Inc., 2012), pp. 495–521.

- ⁶¹ A. Vallée and Y. Lecarpentier, *Cell Biosci.* **9**, 1 (2019).
- ⁶² N. Tandon, C. Cannizzaro, E. Figallo, J. Voldman, and G. Vunjak-Novakovic, in *Annu. Int. Conf. IEEE Eng. Med. Biol. - Proc.* (2006), pp. 845–848.
- ⁶³ J.T. Rubinstein, C.A. Miller, H. Mino, and P.J. Abbas, *IEEE Trans. Biomed. Eng.* **48**, 1065 (2001).
- ⁶⁴ C.A. Erickson and R. Nuccitelli, *J. Cell Biol.* **98**, 296 (1984).
- ⁶⁵ J. Han, Q. Wu, Y. Xia, M.B. Wagner, and C. Xu, *Stem Cell Res.* **16**, 740 (2016).
- ⁶⁶ J.W. Smyth, T.T. Hong, D. Gao, J.M. Vogan, B.C. Jensen, T.S. Fong, P.C. Simpson, D.Y.R. Stainier, N.C. Chi, and R.M. Shaw, *J. Clin. Invest.* **120**, 266 (2010).
- ⁶⁷ L.L.Y. Chiu, R.K. Iyer, J.P. King, and M. Radisic, *Tissue Eng. - Part A* **17**, 1465 (2011).
- ⁶⁸ J.L. Jones, R.E. Jones, and G. Balasky, *Am. J. Physiol.* **253**, H1418 (1987).
- ⁶⁹ R. Visone, G. Talò, S. Lopa, M. Rasponi, and M. Moretti, *Sci. Rep.* **8**, 1 (2018).
- ⁷⁰ Q.X. Xiu, Y.S. Set, W. Sun, and R. Zweigerdt, *Stem Cells* **27**, 2163 (2009).
- ⁷¹ P. McDermott, M. Daood, and I. Klein, *Am. J. Physiol. - Hear. Circ. Physiol.* **18**, (1985).
- ⁷² C.T. Ivester, W.J. Tuxworth, G. Cooper IV, and P.J. McDermott, *J. Biol. Chem.* **270**, 21950 (1995).
- ⁷³ W.W. Sharp, L. Terracio, T.K. Borg, and A.M. Samarel, *Circ. Res.* **73**, 172 (1993).

Table Captions

Table 2. Electrical properties of the three domains within the MPS.

Figure Captions

Figure 1 Design and cell culture model of the microfluidic platform for the generation and maturation of highly anisotropic cardiac tissue. (a) Schematic representation of the microfluidic device including the cell chamber (red), the media channels (blue), and the stimulation electrodes (dark gray). (b) Photo of the assembled microfluidic platform. (c) Detailed schematic view showing the patterned substrate created with electrospun fibers in the cell chamber and how the cardiac cells follow its orientation. A detail of micropost geometry and dimensions is also provided. (d) Experimental timeline.

Figure 2 Electrospun fibers characterization. (a,b) Field emission scanning electron microscopy (SEM) images showing the morphology of the aligned and random fibers, respectively. (c,d) FFT analysis of the nanofiber orientation based on the SEM images. (e) Mean nanofiber diameter for each of the conformations. (f) Characteristic stress-strain curves obtained for the tensile mechanical assay of each sample type. Scale bar in (a,b) = 20 μm . Data in (e) expressed as mean \pm standard deviation ($n = 18$) with **** $p < 0.0001$ (evaluated with Student's t-test).

Figure 3 Electrical finite element model results. (a) Layout and materials composing the different parts of the system: cell chamber filled with culture media, PDMS frame and posts, and four stainless-steel electrodes. The red line indicates the section across which the electrical field was computed ($z = 75 \mu\text{m}$). (b) Electrical field intensity corresponding to the transversal section previously indicated decomposed in its different components (x,y,z) for an input voltage of 5 V_{pp} . (c) Electrical field vectors in a cross-section of the cell chamber ($z = 75 \mu\text{m}$), indicative of the direction of current flow.

Figure 4 Electrical characterization of the device. (a) The experimental setup used to perform the voltage measurements. (b) Comparison of the theoretical curve obtained in

the simulations of the electrical potential with respect to the experimental voltage measurements (red dots). (c) Schematic of the device showing the section for which the electric potential was calculated in the simulations ($z = 75$) and the three holes performed in the cell chamber of the device to obtain the experimental measurements. Experimental data in (b) expressed as mean \pm standard deviation ($n = 3$). Note that the error bars cannot be seen because of the really small deviations: ± 0.03 V for points number 1,2 and ± 0.02 for point number 3.

Figure 5 Immunofluorescence staining of the cardiac tissue and quantification of orientation and gap junctional proteins expression. (a) Fluorescent microscope images of the random electrospun fibers containing rhodamine B (red) and the cardiomyocytes seeded on top stained for the contractile protein troponin T (green), gap junctional protein connexin-43 (red), and cell nuclei (blue) after 7 days in regular culture. (b) Fluorescent microscope images of the aligned electrospun fibers containing rhodamine B (red) and the cardiomyocytes seeded on top stained for the contractile protein troponin T (green), gap junctional protein connexin-43 (red), and cell nuclei (blue) after 7 days in culture (5 of them with electrical stimulation). Scale bar in (a,b) = 40 μm (20 μm in magnification view). (c) Polar plot of the differences in the orientation between the cardiomyocytes seeded on top of the aligned vs random electrospun substrates. Results represent the normalized mean values distribution ($n = 6$) for different angles between -90° to 90° . (d) Analysis of the number of measured Cx-43 gap junctional protein (Cx-43) dots per cell. Results are expressed as mean \pm standard deviation ($n = 6$) with $*p < 0.05$ (evaluated with Student's t-test).

Figure 6 RT-qPCR analysis of the transcriptional expression of different cardiac markers: (a) Connexin-43 (encoded by GJA1 gene), (b) Troponin I (encoded by TNNT3 gene) and (c) ratio between myosin heavy chain alpha and beta isoforms (encoded by the MYH7 and MYH6 genes respectively). Gene expression values are computed as fold changes using the ΔCt method and expressed as a ratio concerning the control

condition. Results are expressed as mean \pm standard deviation ($n = 2$) with $*p < 0.05$ (evaluated with Student's t-test).

SUPPLEMENTARY INFORMATION

A Microphysiological System Combining Electrospun Fibers and Electrical Stimulation for the Maturation of Highly Anisotropic Cardiac Tissue.
Adrián López-Canosa^{1,2}, Soledad Perez-Amadio^{1,2,3}, Eduardo Yanac-Huertas^{1,2}, Jesús Ordoño^{1,2}, Romen Rodriguez-Trujillo^{4,5,6}, Josep Samitier^{5,4,2,6}, Oscar Castano^{4,1,2,6,*} and Elisabeth Engel^{1,2,3}

e-mail: oscar.castano@ub.eu

Supplementary Methods

1. Flow simulation and shear stress estimation

A computational model of the flow pattern in our microfluidic platform was developed using the finite element method (FEM) in the software COMSOL Multiphysics 5.5 (Comsol Inc., US). Numerical simulations were performed using the *Creeping Flow* interface, assuming incompressible flow, negligible effect of the inertial forces, and steady-state conditions, resulting in the following form of the Navier-Stokes equations:

$$\nabla \cdot [-p\mathbf{I} + \boldsymbol{\tau}] + \mathbf{F}$$

$$\rho \nabla \cdot \mathbf{u} = 0$$

Where ρ is the density of the cell media, u is the velocity vector, p is the pressure, τ is the viscous stress tensor and F is the volume force vector. The fluid was considered cell media, which has equivalent properties to water at 37 °C in terms of density (1 kg m⁻³) and dynamic viscosity (7.8*10⁻⁴ Pa s). Regarding the boundary conditions, the inlet flow for each of the media channels was set to 100 $\mu\text{l h}^{-1}$ and the outlet conditions to atmospheric pressure (1 atm). The rest of the boundaries were set to a no-slip condition. The geometry was discretized with a tetrahedral mesh with approximately 1.8*10⁶ elements and calculated using a direct solver based on the PARDISO method. Mesh sensitivity studies were conducted to ensure consistency of the results.

In order to evaluate the shear stress, an estimation was performed considering a rectangular channel geometry ¹:

$$\tau = \frac{6 \mu Q}{h^2 w}$$

Where μ is the dynamic viscosity of the cell media, Q is the flow rate, h the chamber height, and w the chamber width. Considering that $Q = v A = v (h w)$, the previous expression can be simplified to:

$$\tau = \frac{6 \mu v}{h}$$

From the simulation, we can obtain the v parameter, which is the mean velocity in the cell chamber (approximately $1.5 \cdot 10^{-4} \text{ m s}^{-1}$), which results in a shear stress of:

$$\tau = \frac{6 \mu v}{h} = \frac{6 * 7 \cdot 10^{-4} [\text{Pa s}] * 1.5 \cdot 10^{-4} [\text{m s}^{-1}]}{150 \cdot 10^{-6} [\text{m}]}$$

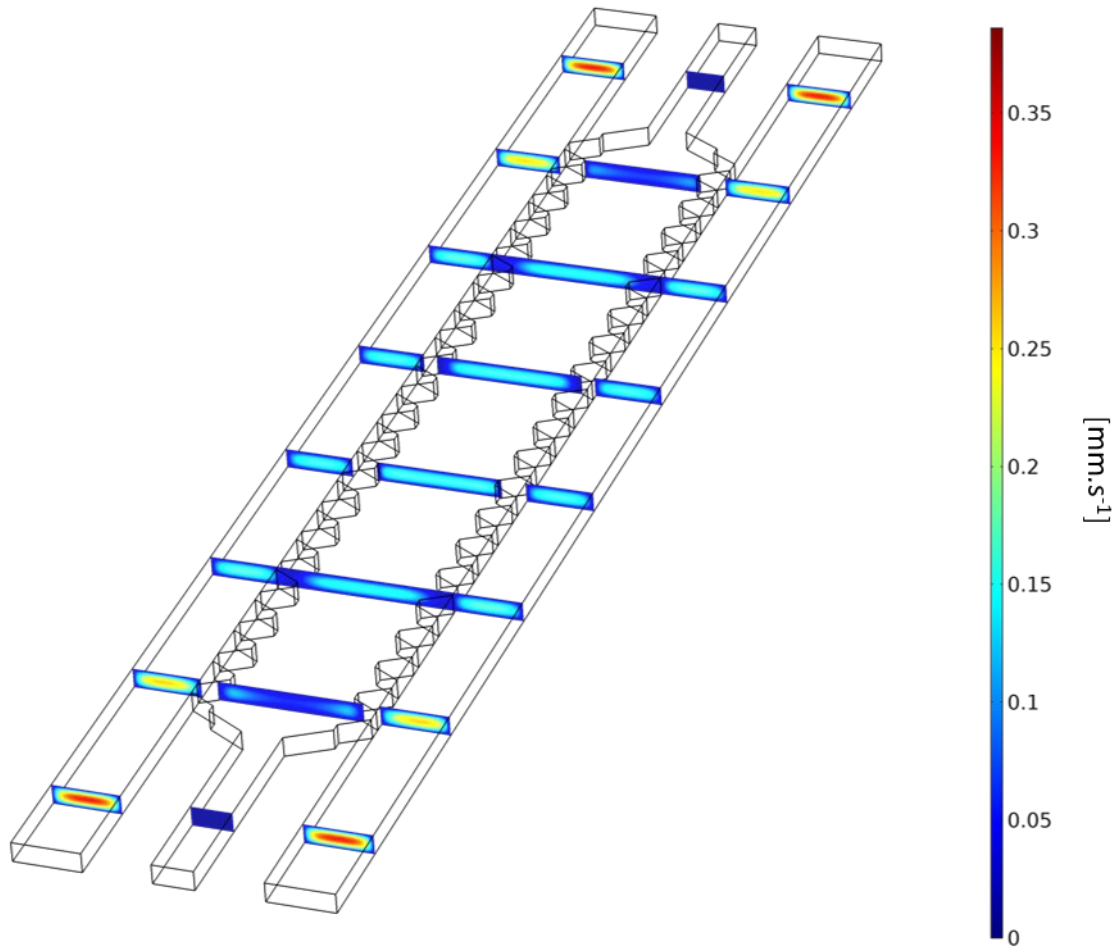
$$\boxed{\tau = 0.004 \text{ Pa} = 0.04 \text{ dyn cm}^{-2}}$$

2. Characterization of myofibroblast activation

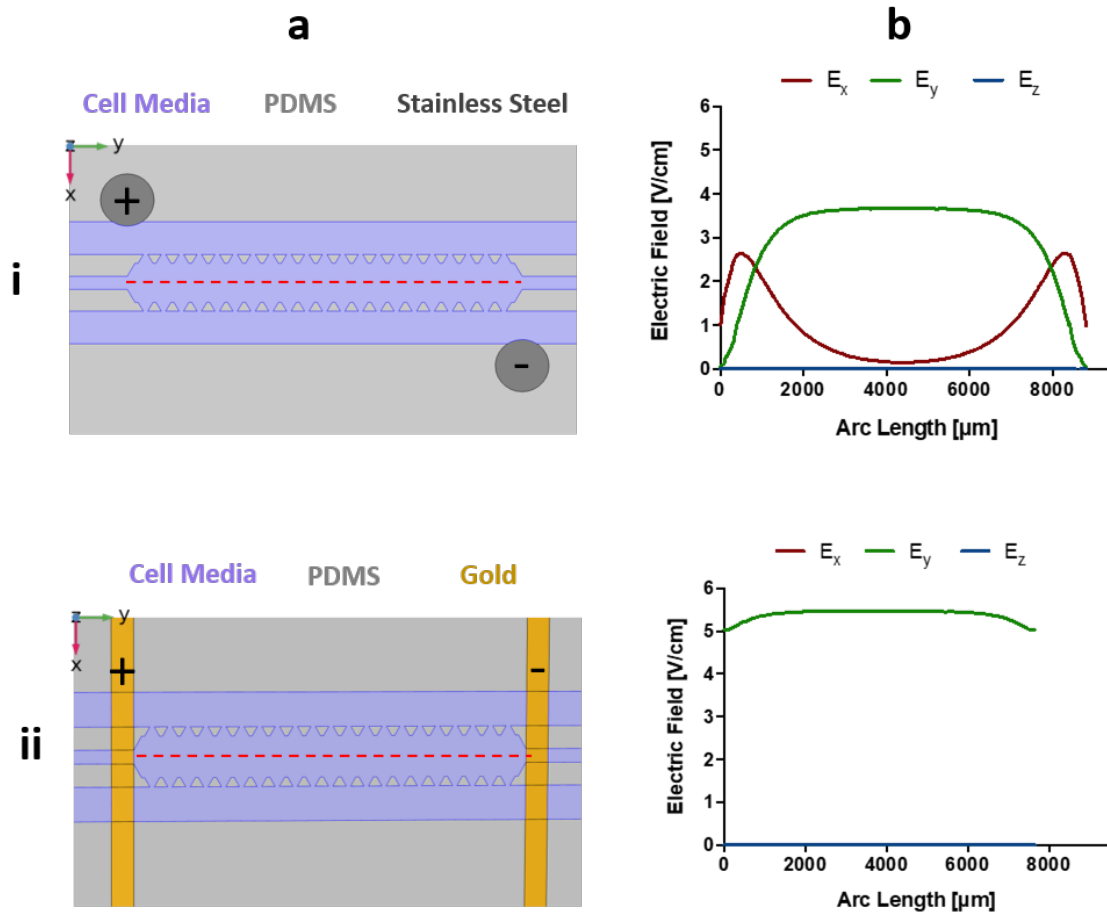
Cardiac cells were isolated following the protocol presented in section 2.5. Cells were seeded in the main cell chamber of the devices (either with random or aligned electrospun PLA fibers) by injecting approximately 10 μl of cell suspension (~100.000 cells/device). Similar cell numbers were also seeded on top of polyacrylamide gels (Young's modulus of 30 kPa) made in a 12-well plate following a previously published protocol ^{2,3}. Cells were incubated at 37 °C for 1 h to allow for cell attachment and then, the chip channels were hydrated by adding 60 μl of cell culture media in each of the reservoirs of one side of the chamber and gently aspirating from the other end with a 1 ml pipette with the tip cut to fit the size of the reservoirs. Each reservoir was then filled with medium (approximately 120 μl) and each of the loaded wells with 500 μl of media. The chips were kept inside a 100 mm Petri dish and maintained along with the Well plate in a 37 °C, 5 % CO₂ incubator with daily changes of media for the duration of the

experiment (3 days). After that time, the cells were fixed and immunostained following the protocol described in section 2.7. For the primary staining, a rabbit polyclonal antibody against smooth muscle myosin heavy chain 11 (Abcam ab125884, UK) was used at 1:200 in the blocking solution. For the secondary staining, Alexa 635 against rabbit antibody (Thermo Fisher, US) was used along with phalloidin labeled with Alexa 488 (Cytoskeleton Inc., US) to stain the F-actin filaments, both at 1:200 in the blocking solution. A counterstaining for cell nuclei was also performed incubating DAPI (Thermo Fisher, US) at 1:1000 in PBS-gly. Imaging was performed on a Leica Thunder fluorescence microscope (Leica Microsystems, DE) with the same acquisition parameters for all the samples (exposure time, LED power, etc.), and the obtained images processed using Image J software (NIH, US).

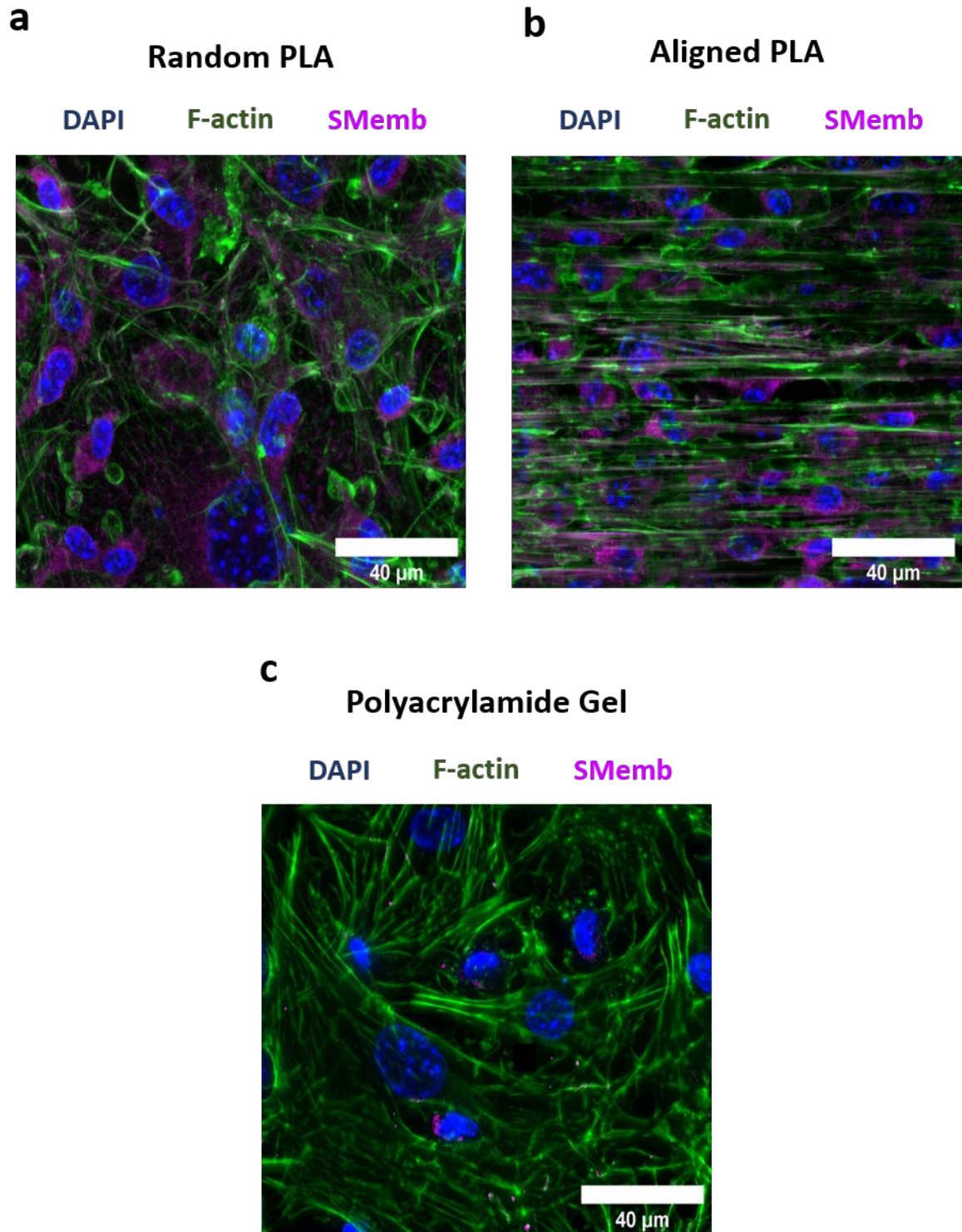
Supplementary Figures



Supplementary Figure 1 Finite element simulation showing the velocity distribution in our microfluidic device (considering an inlet flow of $100 \mu\text{l h}^{-1}$).



Supplementary Figure 2 Electrical finite element model results for different stimulation approaches. (a) Layout and materials composing the different parts of the system for the (i) two stainless steel electrodes and (ii) planar gold electrodes configurations. The red line indicates the section across which the electrical field was computed ($z = 75 \mu\text{m}$). (b) Electrical field intensity corresponding to the longitudinal section previously indicated decomposed in its different components (x,y,z). All results were calculated for an input voltage of $5 V_{pp}$.



Supplementary Figure 3 Immunofluorescence staining of cardiac fibroblasts to evaluate the effect of substrate stiffness in myofibroblast activation. Fluorescent microscope images of cardiac fibroblasts seeded on top of (a) random electrospun PLA fibers (elastic modulus ~ 21 MPa), (b) aligned electrospun PLA fibers (elastic modulus ~ 516 MPa) and (c) compliant polyacrylamide gel (elastic

modulus ~ 0.03 MPa). Staining performed for contractile protein non-muscle myosin heavy chain B (SMemb, in magenta), F-actin cytoskeleton filaments (F-actin, in green), and cell nuclei (DAPI, in blue).

References

- ¹ Y. Son, *Polymer (Guildf)*. **48**, 632 (2007).
- ² T. Yeung, P.C. Georges, L.A. Flanagan, B. Marg, M. Ortiz, M. Funaki, N. Zahir, W. Ming, V. Weaver, and P.A. Janmey, *Cell Motil. Cytoskeleton* **60**, 24 (2005).
- ³ C.E. Kadow, P.C. Georges, P.A. Janmey, and K.A. Beningo, *Methods Cell Biol.* **83**, 29 (2007).